

## FEDSM-ICNMM2010-30161

### INJECTION, TRANSPORT AND REMOVAL OF GAS BUBBLES IN MICROCHANNELS FOR HEAT TRANSFER ENHANCEMENT

**Daniel Attinger**  
Mechanical Engineering  
Columbia University  
New York NY, USA  
da2203@columbia.edu

#### ABSTRACT

Liquid cooling is an efficient way to remove heat fluxes with magnitudes up to  $10,000 \text{ W/cm}^2$ .

One limitation of single-phase microchannel heat transfer is the relatively low Nusselt number, due to laminar flow. Several methods have been used to improve the Nusselt number such as geometric obtrusions, pins and fins and nanofluids. In this talk, we experimentally investigate the heat transfer enhancement of a heat sink where air bubbles are periodically injected. The segmented flow pattern generates recirculation loops that enhance transport phenomena. We show that segmented flow can enhance the Nusselt number of laminar flows in short channels by a factor two. Also, we demonstrate a simple and high-throughput method for removing bubbles from microchannels, using a hydrophobic porous membrane. The role of the thin liquid film coating the bubbles in the heat transfer and the bubble removal is investigated.

#### INTRODUCTION

The concept of a microchannel heat sink was first introduced by Tuckerman and Pease [1] for the purpose of electronic cooling. As Figure 1 shows, a microchannel heat sink is a device that removes heat, by a fluid flowing in channels over a heated substrate (e.g. a computer chip). Tuckerman and Pease optimized the dimensions of the channels in terms of width and height for single-phase flow of water under the constraint of maximum allowable pressure drop and substrate surface temperature. They found that single-phase water-cooling could remove up to  $790 \text{ W/cm}^2$ . This heat flux required a mass velocity,  $G$ , of  $5700 \text{ kg/m}^2\text{s}$  and a pressure drop of  $220 \text{ kPa}$ . A similar optimization process was done by Upadhye and Kandlikar [2], to minimize the pressure drop under the constraints of a given heat flux and maximum substrate temperature. They found that a water pressure drop below  $10$

kPa was sufficient to remove  $100 \text{ W/cm}^2$  with an optimum channel geometry. One problem with single-phase flow heat transfer in microchannels is the low Nusselt number obtained in laminar flow [3], on the order of 4. Methods for increasing the Nusselt number include: surface area enhancement [4, 5] by geometric obtrusions, tree-like bifurcating channels [6], large aspect ratio channels [1, 7], serpentine channels to promote mixing and turbulence [8], short channels where the entrance region dominates [9, 10], nano-fluids [11, 12], and two-phase flow [4, 7, 13-17].

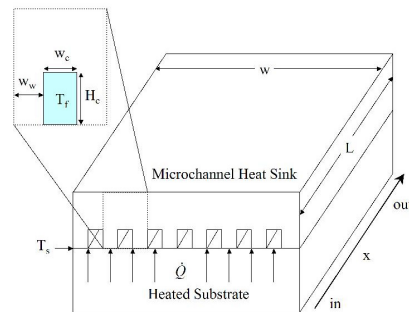


**Figure 1: A microchannel heat sink in direct contact with a heated substrate (such as an integrated circuit chip).**

There is much interest in two-phase flow heat sinks because the heat of vaporization is very high. It has been shown [18] that flow boiling can dissipate up to  $10,000 \text{ W/cm}^2$  [13, 16], which is 10 times more heat than single-phase flow. While flow boiling is attractive because it delivers high heat flux at the constant temperature of the phase change, it can be difficult to control due to backflow and instabilities. Investigation into controlling the instabilities and backflow include the manufacturing of artificial nucleation sites [19], and inlet restrictions [16, 20, 21]. A drawback of boiling flow,

where water is the working fluid, is that the saturation temperature is higher than the operating temperature of most electronics; the proposed solution is to use refrigerants as working fluids since the boiling temperature is lower than water. Refrigerants, however offer lower cooling capabilities due to a lower specific heat and heat of vaporization.

In this work we investigate segmented flow as a way to enhance single-phase heat transfer with water in microchannels, to be used in cooling loops for microelectronics such as in Figure 2. Bubbles can be generated in microfluidic systems continuously by flow-focusing [22-28] and T-junction configurations [29, 30] or on-demand by thermal heating [31] and piezo actuation [32]. Sometimes unwanted gas pockets can form accidentally due to priming or cavitation. Segmented flow is a periodic pattern of non-condensable bubbles and liquid slugs created at a T-junction by the injection of air in liquid-filled microchannels. The bubbles are typically longer than the channel diameter [33], and the break-up occurs according to the mechanism in [33-36]. Segmented flow [33, 37] has been widely used for chemical engineering applications where it increases mass transfer [38-41]. For instance, Kreutzer et al. determined numerically that the rate of mass transfer in liquid slugs was 10 times the rate of laminar flow [40]. It should accordingly increase heat transfer, due to the same phenomenon of enhanced convection by recirculating wakes in the liquid slugs [40, 42]. It has also been shown that the presence of bubbles increases the pressure drop in the channel due to the Laplace pressure at the liquid gas interface [38, 40], a penalty that needs to be considered.

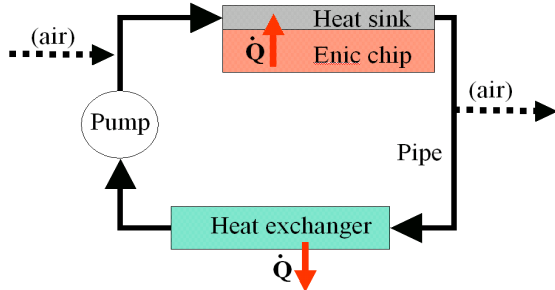


**Figure 2. A liquid cooling loop removes heat from a computer chip. Air bubbles are injected and removed for heat transfer enhancement.**

The presence of bubbles of a non-condensable gas in a heat exchanger presents however an interesting challenge. It may be desired, for industrial applications, to have a closed loop system, where water from the outlet is recirculated through a pump and a heat exchanger to the heat sink inlet, such as in Figure 2. This process might necessitate to remove the air bubbles before the pump and re-inject air after the pump. Various methods have been explored for trapping and removing bubbles from a microchannel, such as dynamic bubble traps [43], and diffusion/capillarity based devices [30, 44-47]. Diffusion-based bubble removal has been successfully demonstrated using a gas-permeable membrane, such as a thin PDMS layer as in [44, 45]. However, the reported gas removal rates are relatively low, typically  $1 \times 10^{-4} \mu\text{L/s}$  per  $\text{mm}^2$  [45]. Alternatively, a porous membrane can be used to separate immiscible fluids, as reported by Kralj and co-workers [48], who achieved complete separation of organic-aqueous and fluorine-aqueous liquid/liquid systems in a microfluidic

device, and provided two design criteria for successful separation. Gas/liquid separation using porous membrane has also been reported [30, 46, 47, 49, 50]. For example, Zhu [46] demonstrated that hydrophobic and hydrophilic membranes can be used together in the end of a microchannel to achieve a complete gas/liquid separation by letting gas and liquid flow through hydrophobic and hydrophilic membranes respectively, but the study did not mention the gas removal rate. He also achieved incomplete separation by using a hydrophilic membrane in a channel flown with a gas/water mixture. Similarly, Kamitani [49] used a hydrophilic porous membrane to enhance liquid filling through the membrane and gas detachment from the membrane in a direct methanol fuel cell. In terms of modeling, several studies have performed calculations of leakage pressure [46, 48, 51]. In this work, we design and demonstrate a high-rate bubble removal system, and provide related physics-based design rules. Our design integrates a hydrophobic membrane into a microfluidic chip and successfully separate gas plugs from a segmented flow. We show that four criteria need to be simultaneously satisfied in order to achieve completed separation of the gas from the liquid.

## NOMENCLATURE

A = area ( $\text{m}^2$ )  
 B = hydraulic coefficient  
 Ca = capillary number ( $\mu\text{v}/\sigma$ )  
 c = specific heat ( $\text{J/kgK}$ )  
 C = gas constant  
 d = hydraulic diameter (m)  
 f = volumetric flow rate ( $\text{m}^3/\text{s}$ )  
 fr = friction factor  
 G = mass velocity ( $\text{kg}/\text{m}^2\text{s}$ )  
 h = convection coefficient ( $\text{W}/\text{m}^2\text{K}$ )  
 H = height (m)  
 k = thermal conductivity ( $\text{W}/\text{mK}$ )  
 K = minor loss term  
 L = length (m)  
 n = number of bubbles  
 N = number of channels  
 p = pressure (Pa)  
 P = perimeter (m)  
 Pr = Prandtl Number ( $\nu/\alpha$ )  
 Nu = Nusselt Number ( $hd/k$ )  
 Re = Reynolds Number ( $\rho U d/\mu$ )  
 $\dot{Q}$  = heat flow (W)  
 $q''$  = heat flux ( $\text{W}/\text{m}^2$ )  
 T = temperature ( $^\circ\text{C}$ )  
 t = time (s)  
 v = velocity (m/s)  
 V = volume ( $\text{m}^3$ )  
 w = width (m)

## Greek Symbols

$\alpha$  = fin enhancement factor  
 $\alpha^*$  = aspect ratio  
 $\beta$  = temperature difference ( $^\circ\text{C}$ )  
 $\delta$  = film thickness (m)  
 $\epsilon$  = liquid fraction

$\kappa$ =permeability (m<sup>2</sup>)  
 $\eta$ = fin efficiency  
 $\theta$  = thermal resistance (K/W)  
 $\mu$ = viscosity (Pa·s)  
 $\rho$ = density (kg/m<sup>3</sup>)  
 $\sigma$  = surface tension (N/m)

### Subscripts

B = bubble  
 c = channel  
 G= gas  
 L = liquid  
 S = surface  
 seg = segmented flow  
 sin = single phase flow  
 slug = liquid slug  
 sub = substrate  
 w= wall

### Theory

To estimate the thermal performance of the heat sink in Figure 1, the equivalent resistances method of Tuckerman and Pease [1] can be used. The total thermal resistance  $\theta_{\text{total}}$  is the ratio of  $\Delta T = T_{S,\text{max}} - T_{L,\text{in}}$ , the difference between the maximum heated substrate temperature and the fluid temperature at the inlet, over the power dissipated,  $\dot{Q}$ . The total thermal resistance,  $\theta_{\text{total}} = \theta_{\text{heat}} + \theta_{\text{conv}}$ , is the sum of a heat resistance and a convective resistance. The heat resistance  $\theta_{\text{heat}} = 1/(c_L f_L)$  is due to the heating of the fluid as it passes through the heat sink; it depends on volumetric flow rate  $f_L$  and specific heat capacity of the fluid  $c_L$ . The symbol  $\theta_{\text{conv}}$  is the resistance of the coolant fluid to heat convection. The expression for  $\theta_{\text{conv}} = (2/kL\text{Nu}L_c w)(w_c/\alpha\eta)$  is derived in [1] by treating the rectangular walls of a micro heat sink as fins with adiabatic boundary conditions at their end, with  $\eta$  the fin efficiency. The symbol  $L_c$  is the channel length,  $w$  is the heat sink width,  $w_c$  is the channel width,  $w_w$  is the width between the channels,  $H_c$  is the channel height and  $\alpha = 2H_c/(w_w + w_c)$  is the fin enhancement factor. From that modeling, the outlet temperature of the fluid and the maximum temperature of the substrate surface can be found based on the power dissipated  $\dot{Q}$  and the inlet temperature of the fluid, as shown in Eq. 1 and 2.

$$T_{L,\text{out}} = (\dot{Q}\theta_{\text{heat}}) + T_{L,\text{in}} \quad (1)$$

$$T_{S,\text{max}} = (\dot{Q}\theta_{\text{conv}}) + T_{L,\text{out}} \quad (2)$$

Several correlations are available for the Nusselt number and pressure drop. For single-phase, laminar, fully developed flow in rectangular channels with constant heat flux boundary conditions, Nu is calculated according to the correlation in [3]: In the case of square channels, this correlation yields  $\text{Nu} = 3.61$ . The Nusselt number of single phase flow is expected to increase at higher Re due to the increasing thermal entry length. When the thermal entry length is no longer negligible, Nu can be found using a correlation by Lee and Garimella [10]. This correlation is valid for rectangular channels of any aspect ratio, constant heat flux boundary conditions, and laminar, hydrodynamically developed flow. When the hydrodynamic

entry region is no longer negligible, correlations by Muzychka and Yovanovich [52] can be used to find Nu. Their work is valid for  $\text{Pr} > 0.1$ , uniform heat flux and constant surface temperature, and any channel cross-sections.

The pressure drop for single-phase flow is found using the Churchill correlation valid for both laminar and turbulent flow [53], where  $d$  is the hydraulic diameter,  $K$  is the minor loss term and  $UL$  is the liquid velocity:

$$\Delta p = \rho (4\text{fr}L_c/d + K)UL^2/2 \quad (3)$$

For segmented flow, Nu at constant heat flux is estimated with a correlation established from detailed multiphase flow simulations in cylindrical pipes by Lakehal et al. [39].

$$\text{Nu}_{\text{seg}} = \text{Nu}_{\text{sin}} + 0.022\text{Pr}^{0.4}\text{Re}_{\text{seg}}^{4/5} \quad (4)$$

In the above equation,  $\text{Nu}_{\text{sin}}$  is the Nusselt number for single-phase fully developed liquid flow,  $\text{Pr}$  is based on the properties of the liquid phase, and  $\text{Re}_{\text{seg}} = d\rho_L V_B/\mu_L(L_B/(L_B + L_{\text{slug}}))$ , where  $V_B$  is the bubble velocity and  $L_B$  and  $L_{\text{slug}}$  are the respective length of the bubble and of the liquid slug. Note that this definition is equivalent to the Reynolds number proposed in [39]. Equation 4 is valid for well-defined gas bubbles when  $d$  is on the order of mm,  $\text{Pr} > 1$ ,  $\text{Re}_{\text{seg}}$  is on the order of 1000, and  $300\text{ K} < (T_L)_{\text{mean}} < 340\text{ K}$ . Multiphase flow simulations in [39] revealed two mechanisms that increase Nu: the generation of the bubbles and the circulation in the liquid slugs. Typically, a segmented flow with recirculating wakes can be generated provided the Bond number  $\rho g d^2/\sigma < 3.368$  [33, 40] and the capillary number  $\text{Ca} < 0.04$  [40].

Other correlations for determining the Nusselt number of segmented flow were examined. Kreutzer [40] obtained an expression for Nu from numerical simulation in square channels. Kreutzer's correlation is only valid when there is full circulation in the slugs and was only verified for  $\text{Re} < 300$ . Hetsroni et al. [54] conducted the first experimental work on the heat transfer of gas-liquid flow in microchannel heat sinks. They established correlations for the Nusselt number in triangular channels, valid for negligible entry length and  $\text{Re} < 100$ . In this work, we use the correlation of Lakehal et al. [39], which best reflects our experimental conditions in terms of Re and Ca range, flow patterns and entry length.

The pressure drop in segmented flow can be described with Eq. 5 [38], where a pressure drop term across the bubbles is added to the single-phase pressure drop for the liquid slugs. The pressure drop depends on two measurable quantities: the number of bubbles in a channel,  $n$ , and slug length,  $L_{\text{slug}}$  [38], as per Eq. 5.

$$\Delta p = n \left( \frac{v_B \mu}{d} \right) \left[ \frac{B}{2} \left( \frac{L_{\text{slug}}}{d} \right) + C(3)^{2/3} (\text{Ca})^{-1/3} \right] \quad (5)$$

For square channels the hydraulic coefficient,  $B = 56.91$  is used as well as  $C = 2.39$ , as determined by [55]. The capillary number,  $\text{Ca}$ , is determined by the bubble velocity [40, 42, 56].

$$\text{Ca} = v_B \mu_L/\sigma \quad (6)$$

Parameters in Eq. 4-6, such as  $L_{\text{slug}}$ ,  $L_B$  and  $v_B$ , are available from high-speed visualizations in our experiments. Values of

the pressure drop and Nu obtained by these correlations will therefore be compared with measurements.

We have also used Eq. 4-6 to design the microchannel heat sink. In the design process, the bubble velocity is not known, and we propose the following process to determine  $v_B$  from an assumed water mass velocity  $G_L$ . We first assume a liquid volume fraction,  $\epsilon = 0.5$ , and slug length  $L_s = 0.001$  m, which are representative of our experiments. Assuming that the cross-section of the bubble is constant along its length, the bubble velocity is expressed by mass conservation [40-42].

$$v_B/U_{\text{slug}} = A_c/A_B \quad (7)$$

With the slug velocity defined as  $U_{\text{slug}} = G_L/\epsilon\rho_L$  we obtain:

$$v_B = A_c G_L / (A_B \epsilon \rho_L) \quad (8)$$

The only unknown parameter above is the cross-sectional area of the bubble,  $A_B$ , which can be found in [57] for  $Ca < 0.04$  [40] by assuming a cross-section with a thin, constant film thickness  $\delta$  along the walls and a thicker film at the edges with radius of curvature,  $r = (w_c - 2\delta)/4$ . The film thickness  $\delta$  is a function of the capillary number, Eq. 6, and is expressed by Eqs. 9 and 10 using a correlation based on the simulations of Hazel and Heil [56].

$$\delta = 0.00332w_c, \text{ For } 0.001 < Ca < 0.04 \quad (9)$$

$$\delta = -0.0423e^{(-Ca/5.3092)} - 0.1018e^{(-Ca/0.3343)} + 0.1761 \quad (10)$$

For  $Ca > 0.04$

## Design

A microchannel heat sink was designed in our laboratory to best demonstrate how segmented flow can enhance the Nusselt number in comparison with single-phase flow. The heat transfer enhancement is most noticeable under two conditions: first,  $\theta_{\text{conv}}$  dominates over  $\theta_{\text{heat}}$ , and second, the flow regime is such that there is a large difference between  $\theta_{\text{conv}}$  for segmented and  $\theta_{\text{conv}}$  for single-phase flow. For design purposes, Figure 3 shows how the thermal resistances vary with liquid flow rate for typical channel diameters, with the same base area,  $L = 0.025$  m and  $w = 0.0075$  m and  $w_w = w_c$ . The  $Ca$  transition represents the point where  $Ca = 0.04$ , when the liquid film becomes thicker and the bubble cross-section changes from the non-axisymmetric shape shown in Figure 4 to a more circular cross-section. This results in a dramatic decrease of circulation in the slug [39, 40, 58]. The  $Re$  transition represents the change from laminar to turbulent flow for the liquid flow rate. For  $500 \mu\text{m}$  wide channels, Figure 3 shows that the Reynolds number of the liquid flow must be greater than 60 in order to be in a regime where  $\theta_{\text{conv}}$  dominates over  $\theta_{\text{heat}}$ . For smaller channel geometries, such as  $50 \mu\text{m}$ ,  $\theta_{\text{heat}}$  is the dominant resistance so that changes in Nu would not significantly modify the surface temperature, which is used to experimentally determine the Nusselt number [57]. For larger widths, such as  $2$  mm, values of  $\theta_{\text{conv}}$  are much higher than in the  $500 \mu\text{m}$  microchannel case, resulting in a less efficient heat sink [57].

Design rules for the bubble removal device were found as a result of our experiments and are described at the end of the 'Result' section.

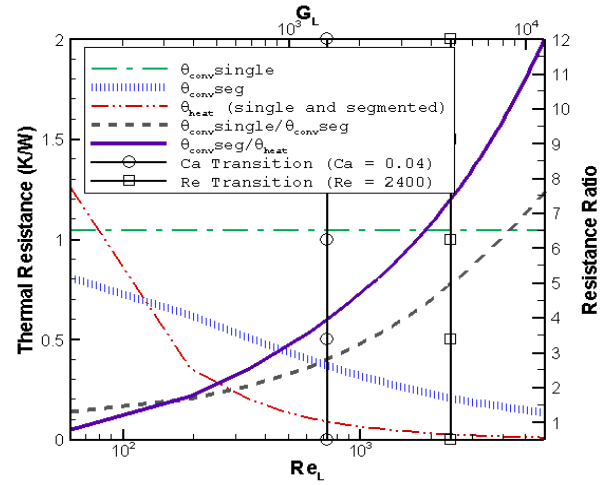


Figure 3. Thermal resistance plotted for a microchannel heat sink with 7 parallel  $500 \mu\text{m}$  channels,  $25$  mm in length.

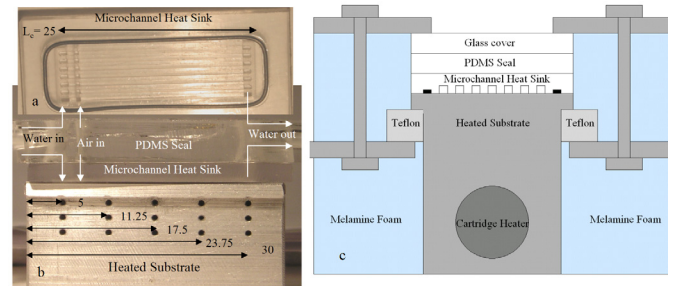


Figure 4. a) Microchannel heat sink with o-ring; b) Test setup with heated substrate showing thermocouple locations, with microchannel heat sink on top (all units are mm) ; c) Cross-sectional view of test section

## Experimental Setup

**Heat sink:** The microchannel heat sink and heated substrate are shown in Figure 4. The heated substrate, made from aluminum, was designed to provide uniform heat flow. Before the single-phase and segmented flow measurements, a simple experiment was performed to quantify the heat loss of the heated aluminum block through the insulation, and verify that the surface temperature of the substrate can be found using a linear interpolation of the thermocouple measurements. The polycarbonate microchannel heat sink was removed, so that the top surface of the aluminum block is exposed to air. The rest of the substrate is insulated with melamine foam approximately  $2$  cm thick. An infrared pyrometer was used to measure the substrate temperature. Since the emissivity of aluminum is very low,  $0.05$ , the surface of aluminum was painted black so that the emissivity was in the range of the pyrometer (a value of  $0.95$  was chosen). The natural convection heat transfer coefficient  $h$  was obtained by a correlation specific to small geometries and dependent on surface temperature, ranging from  $15$ - $25$   $\text{W/m}^2\text{K}$  [59]. Five rows of three K-type thermocouples, as shown in Figure 4b, were used to determine the surface temperature and temperature gradient using linear extrapolation. The test was run at 5 substrate temperatures:



50, 75, 90, 115, 150°C. The maximum heat loss through the insulation was found to be less than 1W, which is negligible compared to the 40 W heat flux we apply during measurements involving fluid flow. The surface temperature was measured with a pyrometer and was found to correspond within 0.5°C to the surface temperatures extrapolated from the set of 5 thermocouple measurements perpendicular to the surface. The standard deviation of the extrapolated values along the surface was less than 0.5°C.

The microchannel heat sink (Figure 4a) was milled from a polycarbonate slab, with a glass transition temperature of 150°C, into seven parallel square channels with respective length and width of 25 mm and 500  $\mu\text{m}$ . Polycarbonate was chosen since it is transparent and easy to manufacture. The heat sink was pressed on top of the heated substrate and sealed with an O-ring. It was heated with a constant power of 40W and the water flow rate was varied from 238 – 3095  $\text{kg/m}^2\text{s}$ .

The heated substrate and microchannel heat sink were insulated with melamine foam, as shown in Figure 4c, with a typical loss measured to be less than 1W. The water was pumped with a peristaltic pump, and the liquid mass velocity  $G_L$  was found by measuring the fluid volume at the outlet over time. Bubbles were generated by injecting air through a slit at constant pressure using a Druck DPI 530 pressure regulator (2 bar, precision  $\pm 1\%$  FS). The pressure was varied depending on  $G_L$  to produce a liquid fraction close to 0.5. The pressure drop along the channel was measured with a pressure transducer (Honeywell, 105.53 kPa,  $\pm 0.61$  kPa uncertainty, 100  $\mu\text{s}$  response time). Thermocouples (Type K, 0.5 mm diameter, Omega, 100ms response time,  $\pm 0.5^\circ\text{C}$  uncertainty) recorded inlet and outlet temperatures of the fluid, along with 15 measurements on the substrate, as shown in Figure 4b.

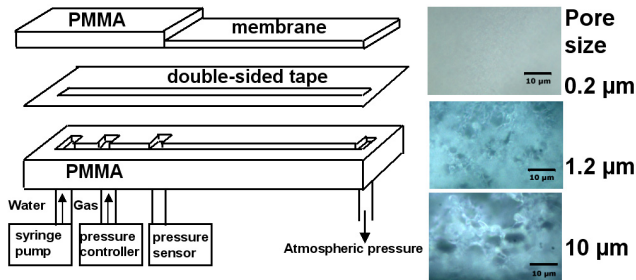


**Figure 5: (Left) Assembly of bubble removal chip. A 500  $\mu\text{m}$  wide slit is cut through the tape, and aligned on top of the main channel. Bubbles are generated at a T-junction, where water is pushed by syringe pumps (KDS 210) and the gas pressure is controlled by a pressure regulator. The generated bubbles are then transported to the porous membrane, where extraction takes place. (Right) Micrographs of porous hydrophobic membranes with different pore sizes.**

**Degasser:** The gas removal device is shown in Figure 5. The microchannels are 500  $\mu\text{m}$  wide and 500  $\mu\text{m}$  deep. They are milled out from a PMMA (Polymethylmethacrylate) slab using a micromilling machine, with less than 500 nm surface roughness. The channels are then sealed with PMMA, a 200  $\mu\text{m}$  thick hydrophobic acrylic copolymer membrane (Pall Corporation), and 70  $\mu\text{m}$  thick double-sided tape (Adhesives Research, Inc), as shown in Figure 5. The tested porous hydrophobic membranes had three respective typical pore

sizes, 0.2, 1.2 and 10  $\mu\text{m}$  (Figure 5). A 500  $\mu\text{m}$  wide slit is cut through the tape, and aligned on top of the main channel. Therefore, the bubble generation section has all four walls made of PMMA while the gas removing section has a channel made of three PMMA walls and one membrane wall, if we neglect the presence of the tape. This gas removal device is tested with bubbles produced according to a similar injection process as described for the heat sink above. A piezoresistive pressure sensor (Honeywell ASCX15DN, 103.4 kPa differential, repeatability  $\pm 0.2\%$  FS) is used to monitor the pressure difference between the atmosphere and the fluid upstream of the hydrophobic membrane.

## Results

**Heat sink:** Convective heat transfer measurements in the heat sink were made at constant heating power of 40W, and with water flow rates between 35-300 mL/min, corresponding to water mass velocities  $G_L$  of 300-3000  $\text{kg/m}^2\text{s}$  and  $\text{Re}_L$  from 160-1580, where  $\text{Re}_L$  is defined as  $G_L d/\mu_L$  for both single phase and segmented flow. Neglecting the low thermal losses through the insulation, the enthalpy change of the fluid can be replaced by the power supplied by the heater. An energy balance surrounding the channel provides the convection coefficient, h:

$$\dot{Q}_{\text{heater}} = (2\eta H_c + w_c) N h \int_0^L \beta dx \quad (11)$$

Where  $\beta$ ,  $\eta$  and  $N$  are the temperature difference between the substrate and the fluid, the fin efficiency and the number of channels, respectively [7]. Since the first and last row of the thermocouples on the heated substrate correspond to the fluid inlet and outlet, the integral is discretized along the fluid flow direction into four sections using the trapezoidal rule. Equation 11 can be rearranged to solve for h as a function of the 5 surface temperatures and the inlet and outlet temperature of the fluid.

The Nusselt number is found from the heat transfer coefficient by  $\text{Nu} = h d/k_L$ , where  $k_L = 0.64 \text{ W/Km}$  is the fluid thermal conductivity. The maximum uncertainty of the Nusselt number is  $\pm 4\%$  due to the propagation of uncertainties in the temperature, geometry and thermal losses through the insulation. A summary of all uncertainties and their sources can be found in [57]. Major contributors to the uncertainty are the thermocouple measurements and the heat flow measurement. For example, at  $G_L = 1140 \text{ kg/m}^2\text{s}$ , the average temperature difference  $\beta$  is  $20^\circ\text{C}$  with an uncertainty of  $\pm 0.5^\circ\text{C}$ , or  $\pm 2.5\%$ . Also, section 4 showed that the uncertainty of  $\dot{Q}_{\text{heater}}$  due to heat losses is less than 1 W, i.e.

2.5 %. Figure 6 shows that segmented flow increases the dimensionless heat transfer coefficient Nu up to 140% over single phase flow, for values of  $G_L < 2000 \text{ kg/m}^2\text{s}$ , in very good agreement with the numerically obtained correlation of [39]. For flow rates higher than  $2000 \text{ kg/m}^2\text{s}$  (or  $\text{Re}_L \sim 1000$ ), the heat transfer enhancement due to the segmented air bubble flow decreases quickly, and at  $G_L > 2500 \text{ kg/m}^2\text{s}$  ( $\text{Re} = 1200$ ), the bubbles have no more influence on the heat transfer process. Interestingly, this transition starts at flow rates where the capillary number reaches the transition value of 0.04 (shown by a vertical bar), and the flow visualizations in Table 1 and [57] confirm a transition to churn flow. This might indicate that segmented flow enhances heat transfer

provided the film between bubbles and wall does not become too thick, which would weaken the recirculation wakes. As a side note, we were only able to produce segmented flow for values of  $G_L$  between 330 and 2850  $\text{kg/m}^2\text{s}$ . At lower  $G_L$  values segmented flow is replaced by bubbly flow (i.e. bubbles with diameters smaller than the channel diameter), and at higher  $G_L$  values a churn flow appears (fast bubbles with thick films,  $Ca$  reaching 0.04 and above, no heat transfer enhancement), in agreement with the data compiled by [33, 60]. The increasing values of the Nusselt numbers for single phase flow at larger flow rates are very likely due to the non-negligible thermal and hydrodynamic entry lengths. For instance, the correlations of Lee and Garimella [10] can be used to calculate  $Nu$  for thermally developing flow. In our experiments the thermal entry region accounts for 10% of the channel length at  $Re = 30$ . These correlations are only valid until  $Re \sim 100$ , when the hydrodynamic entry becomes non-negligible. For cases where both thermal and hydrodynamic entry length are significant, the correlation of Muzychka and Yovanovich [52] should be used. Predictions from this correlation agreed very well with our experimental values for  $Re > 100$  [52].

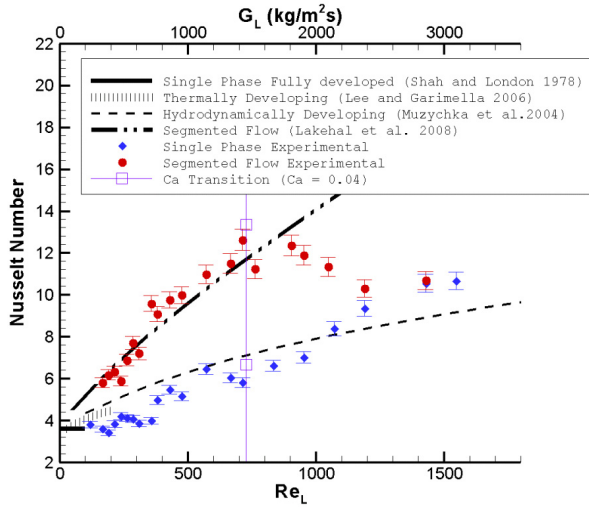


Figure 6. Theoretical and measured values of Nusselt number for single phase and segmented flow versus the Reynolds number based on the mass velocity of water.

The penalty in pressure drop associated with segmented flow is evaluated in Figure 7, which shows that segmented flow exhibits pressure drops higher than single phase flow at the same prescribed liquid mass velocity, as predicted by the correlations in [38]. The segmented flow heat transfer enhancement scheme that we present here would only be of interest if it provides a higher Nusselt number than single phase flow, for the same pressure drop. This is verified in Figure 7 for pressure drop values ranging from 5 to 30 kPa, where the Nusselt number enhancement is about 50% using segmented flow rather than single phase flow, for the same amount of pressure drop.

Case	b	c
$G_L$ ( $\text{kg/m}^2\text{s}$ )	380.95	1333.33
Flow Regime	slug	slug

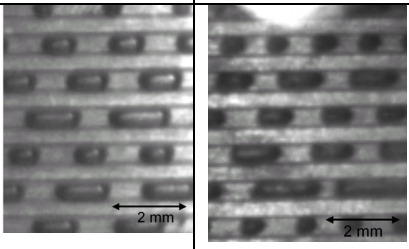
Average $L_B$ (mm)	1.16	1.04
Average $L_{\text{slug}}$ (mm)	0.93	0.79
$\epsilon$	0.482	0.47
Increase in $\Delta p$ (kPa)	2.26	9.81
Visualization		

Table 1. Visualization of two cases of segmented flow with corresponding flow parameters.

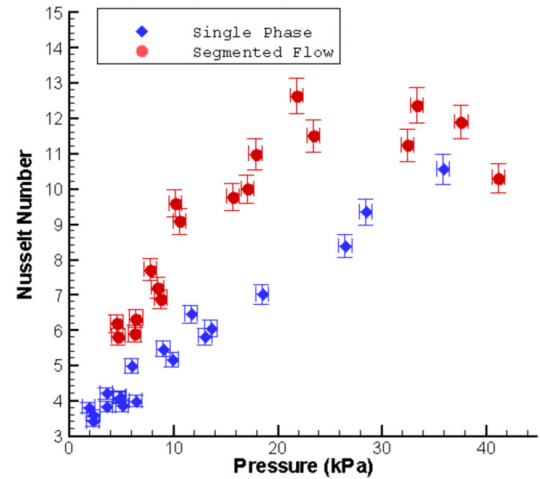


Figure 7. Nusselt number expressed as a function of the pressure drop for single phase and segmented flow.

**Degasser:** As for the bubble trapping device, several prototypes were built according to the design presented above. The devices worked satisfactorily provided the two following outcomes were avoided: membrane water leakage and incomplete bubble extraction. During incomplete extraction, the outflow is not pure water but an air-liquid mixture. During membrane leakage, water and gas flow through the membrane. Our analysis below shows that four criteria, as listed in Table 2, need to be simultaneously satisfied to guarantee complete gas extraction without membrane leakage.

For instance, the geometry of our bubble trap requires a bubble length larger than the channel height for putting bubble and membrane in contact, thus allowing for degassing. This is the first necessary criterion for complete gas extraction, criterion 1 in Table 2.

Criterion	Equation
1. Bubble length $L_{bubble}$ needs to be larger than the channel height $H$ .	$L_{bubble} > H$
2. Bubble traveling time on a membrane that has a length of $L$ should be sufficient to transport all the gas through the membrane. $\Delta p$ =pressure difference across mambrane.	$L/v > \tau = H \frac{\mu}{\kappa} \frac{h}{\Delta p - \frac{4\gamma}{H}} \ln\left(\frac{l_0}{l_1}\right)$
3. Bubble speed $v$ should be lower than a critical value: otherwise a stable liquid film between the bubble and the membrane prevents mass transfer.	$v < v_{c\_membrane} = \frac{1}{9\sqrt{3}} \frac{\gamma/\mu}{a} \theta_{E\_membrane}^3$
4. The pressure difference across the membrane $\Delta p$ should be smaller than the Laplace pressure $\Delta p_{LP}$ to prevent water leakage.	$\Delta p < \Delta p_{LP} = -\frac{4\gamma \cos \theta}{d}$

**Table 2: These four criteria need to be simultaneously satisfied to successfully remove gas bubbles from microfluidic channels**

A second criterion can be formulated by considering the time needed to fully extract the gas bubble. We can equal the shrinking rate of the bubble  $dV/dt$  to the gas flow rate  $Q$  through the membrane, which can be estimated by Darcy's law:

$$-\frac{dV}{dt} = Q = \frac{\kappa}{\mu} \frac{p_B - p_0}{h} \frac{V}{H}, \quad (12)$$

where  $V/H$  gives the contact area between the bubble and the membrane,  $\kappa$  is the membrane permeability. Symbols  $p_B$  and  $p_0$  are respectively the pressure in the bubble and the atmospheric pressure. In the experiment,  $p_B$  is estimated by  $p_L + 1/2 \cdot (2\gamma/r_1 + 2\gamma/r_2)$ , where  $p_L$  is the measured liquid pressure and  $r_1$ ,  $r_2$  are the radii of curvature measured at the bubble head and tail respectively. Assuming that the bubble shrinks by reducing its length keeping its pressure and height constant, we can integrate to determine the extraction time  $\tau$ :

$$\tau = H \frac{\mu}{\kappa} \frac{h}{p_B - p_0} \ln\left(\frac{l_0}{l_1}\right) \quad (13)$$

where  $l_0$  and  $l_1$  are the initial bubble length and final bubble length respectively. This integral does not converge to a finite time, but a reasonable estimate of the bubble extraction time is obtained by assuming a small value  $l_1$  of 1% of the channel height. However, Equation (13) is not very convenient to be used for design purposes, because it requires knowledge of the bubble curvature and of the pressure, rather than just an estimate of the pressure in the liquid  $p_B$ . We observe that the Laplace contribution is bounded to a range, i.e.  $-4\gamma/H$  to  $4\gamma/H$ , with a worst-case scenario happening when  $p_B = p_L - 4\gamma/H$ , because a lower pressure in the bubble always slows down the bubble removal. Therefore, for design purposes, we use can estimate  $p_B$  as  $p_L - 4\gamma/H$  as listed in Table 2.

For the membranes with 1.2 and 10  $\mu m$  pores, the theoretical  $\tau$  can be on the order of milliseconds, thus this criterion

suggests that gas bubbles can be removed from very fast flows, at speed on  $10^4$  m/s, much faster than in the experiments described here. This situation is unrealistic because of the coating liquid films surrounding bubbles traveling in channels at non-negligible capillary numbers. In this case, a third criterion has to be formulated for complete gas removal to account for the liquid film between the wall and the gas plug, which might delay or compromise gas extraction. A static gas/water interface would contact the wall with a contact angle  $\theta_E$  and form a clear triple line. However, an interface moving along the wall will exhibit a dynamic contact angle  $\theta_D$ , which decreases for increasing bubble velocities. There is therefore a critical velocity, where the wetting angle approaches zero, and above which a film appears between the plug and the wall because the triple line cannot find a stable position anymore. The critical velocity  $v_c$ , can be estimated by [61]:

$$v_c = \frac{1}{9\sqrt{3}} \frac{\gamma/\mu}{a} \theta_E^3 \quad (14)$$

where  $a = 20$  is a dimensionless coefficient that only weakly depends on  $v$ . For an air-water system in respective contact with PMMA and membrane surfaces,  $v_c$  is calculated to be 0.38 and 2.3 m/s, respectively, using contact angles measured in [62]. Once the film is formed, the thickness  $e$  of the film can be calculated as [61]  $e = d/2 \cdot Ca^{2/3}$ , where  $d$  is the channel diameter and  $Ca$  is the capillary number. Assuming  $d$  as the hydraulic diameter of our channel, Figure 8 (second y-axis) shows the theoretical film thickness  $e$  as a function of bubble speed  $v$  on both PMMA and membrane surfaces.

In our experiment, bubbles travel along the PMMA wall and then on the membrane so that the corresponding film situations occur. If the bubble speed  $v$  is greater than  $v_{c\_membrane}$ , a stable film between the bubble and the membrane will prevent gas removal. On the other hand, if the bubble speed  $v$  is smaller than  $v_{c\_membrane}$ , the film might become unstable on top of the membrane and rupture so that gas can be removed, provided the membrane is long enough. In the experiments reported using first y-axis in Figure 8, we see that gas plugs that are slower than  $v_{c\_membrane}$  can be completely extracted at certain locations in the channel, a situation that was not achieved for gas plugs that are faster than  $v_{c\_membrane}$ . Note that, the bubble travel distance generally increases with the bubble velocity, however the data points look scattered. This may be due to the nonuniformity of the pore sizes and nonhomogeneous distribution of the pores on the membrane surface, as pictured in Figure 5. Though the definition of surface roughness of porous media is not very straightforward [63], we believe that the rough surface topology of the membrane can have three major effects: 1) surface roughness tends to increase the macroscopic contact angle, or apparent contact angle [61]. Therefore, we measured the macroscopic contact angle from a sessile drop on the membrane and used this measured value in Equation 5; 2) the air-filled pores under the membrane surface tend to promote film rupture on the membrane surface [64]; 3) surface roughness can cause contact line pinning and depinning during advancing and receding [65]. While these three effects add complexity to

our physical model, the approximation in Criterion 3 is meaningful, and sufficient to provide guidance for design purposes.

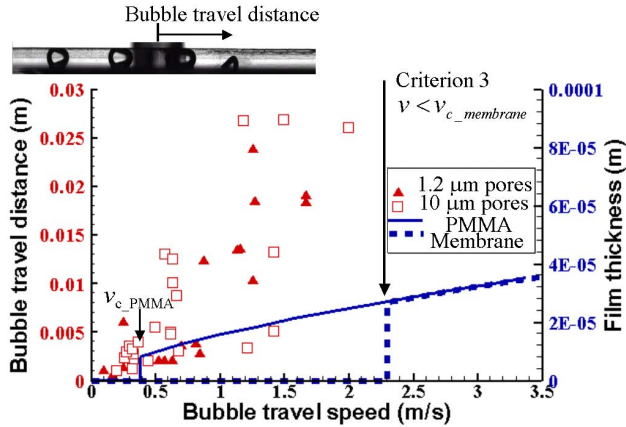


**Figure 8: Experimental maximum bubble travel distance and theoretical film thickness as functions of bubble travel speed.**

For the bubbles that are slower than  $v_{c\_membrane}$  can be completely extracted at certain locations in the channel, a situation that was not achieved for bubbles that are faster than  $v_{c\_membrane}$ . Note that, the bubble travel distance generally increases with the bubble travel speed, however the data points look scattered. This may be due to the nonuniformity of the pore sizes and nonhomogeneous distribution of the pores on the membrane surface, as pictured in Figure 5.

A porous hydrophobic membrane will prevent the water-air meniscus to go through the pores because of interfacial tension, a situation analyzed in [48] for a liquid/liquid system. Using the same principle, we formulate a criterion necessary to prevent water from leaking through a porous hydrophobic membrane. As the air-liquid meniscus is pinned at the entrance of the pore and the surface tension, it holds the pressure difference across the meniscus and prevents water from leaking through the pore. However, with an increasing pressure difference, the angle between the meniscus and the inner wall of the pores will reach a maximum value of the equilibrium wetting angle. In another word, a meniscus can hold a pressure difference up to a maximum value of  $\Delta p_{LP} = -4\gamma \cos\theta/d$ , where  $\gamma$  is the surface tension between gas and water,  $\theta$  is the contact angle and  $d$  is the pore size [61]. As long as the pressure difference  $\Delta p$  across the membrane is smaller than  $\Delta p_{LP}$ , there will be no water leaking through the membrane, which gives our fourth criterion as listed in Table 2. Comparison between experimental and theoretical leakage values were found in good agreement [62].

## CONCLUSION

Experiments and optimization studies have demonstrated that segmented flow could enhance heat transfer by up to 140% in a microchannel heat sink, in comparison with single-phase flow at the same liquid flow rate. The Nusselt number was used to characterize the improvement in heat transfer. Also, the pressure drop penalty in implementing segmented flow was reasonable, in the sense that, for the same values of pressure drop, segmented flow delivers a higher Nusselt number than single phase flow. We determined that segmented flow would provide an intermediate step between single-phase

and boiling flow for the purpose of electronic cooling. Also, we measured that the heat transfer enhancement only occurs for a specific range of flow rates and capillary numbers. At lower or higher capillary numbers, we explain that no significant heat transfer enhancement is observed because segmented flow is replaced by bubbly or churn flow respectively. Finally, A microfluidic device has been manufactured to separate gas from water in a segmentation flow. Four necessary operating criteria have been determined experimentally and explained theoretically to achieve a complete separation of the gas from the liquid. To further investigate the bubble dynamics and the separation physics, as well as the associated heat transfer, we plan in future work to use computational fluid dynamics to simulate the two-phase flow along and across the porous membrane, in a complex geometry.

## ACKNOWLEDGEMENTS

The author acknowledges the contribution of his graduate students to this work, especially Amy Betz and Jie Xu, as well as the support of the National Science Foundation (Career grant 0449269).

## REFERENCES

1. Tuckerman, D.B. and R.F.W. Pease, *High-Performance Heat Sinking for VLSI*. IEEE Electron Device Letters, 1981. EDL-2(5): p. 126 -129.
2. Upadhye, H.R. and S.G. Kandlikar, *Optimization of microchannel geometry for direct chip cooling using single phase heat transfer*. in *Proceedings of the Second International Conference on Microchannels and Minichannels (ICMM2004)*. 2004.
3. Shah, R.K. and A.L. London, *Laminar Flow Forced Convection in Ducts: A source book for compact heat exchanger analytical data*. Advances in Heat Transfer, ed. T.F. Irvine and J.P. Hartnett. Vol. Supplement 1. 1978, New York: Academic Press.
4. Krishnamurthy, S. and Y. Peles, *Flow boiling water in a circular staggered micro-pin heat sink*. International Journal of Heat and Mass Transfer, 2008. 51: p. 1349-1364.
5. Wang, Y., *Experimental investigation of heat transfer performance for a novel microchannel heat sink*. Journal of Micromechanics and Microengineering, 2008. 18.
6. Escher, W., B. Michel, and D. Poulikakos, *Efficiency of optimized bifurcating tree-like and parallel microchannel networks in the cooling of electronics*. International Journal of Heat and Mass Transfer, 2008. 52: p. 1421-1430.
7. Qu, W. and I. Mudawar, *Flow boiling heat transfer in two-phase micro-channel heat sinks*. International Journal of Heat and Mass Transfer, 2003. 46: p. 2755-2771.
8. Rosaguti, N., *laminar flow and heat transfer in a periodic serpentine channel with semi-circular cross section*. International Journal of Heat and Mass Transfer, 2006. 49: p. 2912-2923.
9. Tiantian, Z. and J. Li, *Laminar flow characteristics in entry region in microchannels*. in *2008 Proceedings*



- of the ASME Micro/Nanoscale Heat Transfer International Conference, MNHT 2008. 2008.
10. Lee, P.-S. and S.V. Garimella, *Thermally developing flow and heat transfer in rectangular microchannels of different aspect ratios*. International Journal of Heat and Mass Transfer, 2006. 49: p. 3060-3067.
11. Lee, J. and I. Mudawar, *Assessment of the effectiveness of nanofluids for single-phase and two-phase heat transfer in micro-channels*. International Journal of Heat and Mass Transfer, 2007. 50(3-4): p. 452-463.
12. Tsai, T.-H. and R. Chein, *Performance analysis of nanofluid-cooled microchannel heat sinks*. International Journal of Heat and Fluid Flow, 2007. 28: p. 1013-1026.
13. Mudawar, I., *Assessment of High-Heat-Flux Thermal Management Schemes*. IEEE Transactions on Components and Packaging Schemes, 2001. 24(2).
14. Steinke, M.E. and S.G. Kandlikar, *An Experimental Investigation of Flow Boiling Characteristics of Water in Parallel Microchannels*. Journal of Heat Transfer, 2004.
15. Agostini, B., M. Fabbri, J. Park, L. Wojtan, and J. Thome, *State of the Art of High Heat Flux Cooling Technologies*. Heat Transfer Engineering, 2007. 28(4): p. 258-281.
16. Kandlikar, S., *High Heat Flux Removal with Microchannels-A Roadmap of Challenges and Opportunities*. Heat Transfer Engineering, 2005. 26(8): p. 5-14.
17. Qu, W. and I. Mudawar, *Measurement and prediction of pressure drop in two-phase micro-channel heat sinks*. International Journal of Heat and Mass Transfer, 2003. 46(15).
18. Mudawar, I. and M.B. Bowers, *Ultra-high critical heat flux (CHF) for subcooled water flow boiling-I: CHF data and parametric effects for small diameter tubes*. International Journal of Heat and Mass Transfer, 1999. 42(8): p. 1405-1428.
19. Kuo, C.-J., A. Kosar, Y. Peles, S. Virost, C. Mishra, and M. Jensen, *Bubble Dynamics During Boiling in Enhanced Surface Microchannels*. Journal of Micromechanics and Microengineering, 2006. 15(6): p. 1514.
20. Kuo, C.-J. and Y. Peles, *Pressure effects on flow boiling instabilities in parallel microchannels*. International Journal of Heat and Mass Transfer, 2009. 52(1-2): p. 271-280.
21. Kosar, A., C.J. Kuo, and Y. Peles, *Suppression of boiling flow oscillations in parallel microchannels by inlet restrictors*. Journal of Heat Transfer, 2006. 128(3): p. 251-260.
22. Sevilla, A., J.M. Gordillo, and C. Martinez-Bazan, *Bubble formation in a coflowing air-water stream*. J. Fluid Mech., 2005. 530: p. 181-195.
23. Hettiarachchi, K., E. Talu, M.L. Longo, p.A. Dayton, and A.P. lee, *On-chip generation of microbubbles as a practical technology for manufacturing contrast agents for ultrasonic imaging*. Lab on a Chip, 2007. 7(4): p. 463-468.
24. Herrada, M.A. and A.M. Ganan-Calvo, *Swirl flow focusing: A novel procedure for the massive production of monodisperse microbubbles*. Physics of Fluids, 2009. 21(4).
25. Hashimoto, M., S.S. Shevkoplyas, B. Zasonska, T. Szymborski, P. Garstecki, and G.M. Whitesides, *Formation of Bubbles and Droplets in Parallel, Coupled Flow-Focusing Geometries*. Small, 2008. 4(10): p. 1795-1805.
26. Gordillo, J.M., Z. Cheng, A.M. Ganan-Calvo, M. Marquez, and D.A. Weitz, *A new device for the generation of microbubbles*. Physics of Fluids, 2004. 16(8): p. 2828-2834.
27. Garstecki, P., I. Gitlin, W. DiLuzio, and G.M. Whitesides, *Formation of monodisperse bubbles in a microfluidic flow-focusing device*. Applied Physics Letters, 2004. 85(13): p. 2649-2651.
28. Cubaud, T., M. Tatineni, X. Zhong, and C.M. Ho, *Bubble dispenser in microfluidic devices*. Physical Review E - Statistical, Nonlinear, and Soft Matter Physics, 2005. 72(3): p. 1-4.
29. Laari, A., J. Kallas, and S. Palosaari, *Gas-liquid mass transfer in bubble columns with a T-junction nozzle for gas dispersion*. Chemical Engineering & Technology, 1997. 20(8): p. 550-556.
30. Gunther, A., M. Jhunjhunwala, M. Thalmann, M.A. Schmidt, and K.F. Jensen, *Micromixing of Miscible Liquids in Segmented Gas-Liquid Flow*. Langmuir, 2005. 21(4): p. 1547-1555.
31. Prakash, M. and N. Gershenfeld, *Microfluidic Bubble Logic*. Science, 2007. 315: p. 832-835.
32. Xu, J. and D. Attinger, *Drop on demand in a microfluidic chip*. Journal of Micromechanics and Microengineering, 2008. 18: p. 065020.
33. Weinmueller, C., N. Hotz, A. Mueller, and D. Poulikakos, *On two-phase flow patterns and transition criteria in aqueous methanol and CO2 mixtures in adiabatic, rectangular microchannels*. International Journal of Multiphase Flow, 2009. 35(8): p. 760-772.
34. Cubaud, T. and C.-M. Ho, *Transport of bubbles in square microchannels*. Physics of Fluids, 2004. 16(12).
35. Gunther, A., S.A. Khan, M. Thalmann, F. Trachsel, and K.F. Jensen, *Transport and reaction in microscale segmented gas liquid flow*. Lab on a chip, 2004. 4: p. 278-286.
36. Menech, M.D., P. Garstecki, F. Jousse, and H.A. Stone, *Transition from squeezing to dripping in a microfluidic T-shaped junction*. Journal of Fluid Mechanics, 2008. 595: p. 141-161.
37. Thorsen, T., R.W. Roberts, F.H. Arnold, and S.R. Quake, *Dynamic pattern formation in a vesicle-generating microfluidic device*. Physical Review Letters, 2001. 86(18): p. 4163-4166.
38. Steijn, V. and M. Kreutzer, *Velocity Fluctuations of segmented flow in microchannels*. Chemical Engineering Journals, 2008. 135S: p. 159-165.
39. Lakehal, D., G. Larrignon, and C. Narayanan, *Computational Heat Transfer and Two-phase*

- Topology in miniature tubes. Microfluid nanofluid, 2008. 4: p. 261-271.
40. Kreutzer, M.T., F. Kapteijn, J.A. Moulijn, and J.J. Heiszwolf, *Multiphase Monolith Reactors: Chemical reaction engineering of segmented flow in microchannels*. Chemical Engineering Science, 2005(60): p. 5895-5916.
41. Chen, W.L., *Gas-Liquid two-phase flow in micro-channels*. International Journal of Multiphase flow, 2002. 28: p. 1253-1247.
42. Thulasidas, T.C., M.A. Abraham, and R.L. Cerro, *Bubble-Train Flow In Capillaries of Circular and Square Cross Section*. Chemical Engineering Science, 1994. 50(2): p. 183-199.
43. Schonburg, M., P. Urbanek, G. Erhardt, B. Kraus, U. Taborski, A. Muhling, S. Hein, M. Roth, H.J. Tiedtke, and W.P. Klovekorn, *Significant reduction of air microbubbles with the dynamic bubble trap during cardiopulmonary bypass*. Perfusion, 2001. 16(1): p. 19-25.
44. Skelley, A.M. and J. Voldman, *An active bubble trap and debubbler for microfluidic systems*. Lab on a Chip - Miniaturisation for Chemistry and Biology, 2008. 8(10): p. 1733-1737.
45. Sung, J.H. and M.L. Shuler, *Prevention of air bubble formation in a microfluidic perfusion cell culture system using a microscale bubble trap*. Biomedical Microdevices, 2009. 11(4): p. 731-738.
46. Zhu, X., *Micro/nanoporous membrane based gas-water separation in microchannel*. Microsystem Technologies, 2009. 15(9): p. 1459-1465.
47. Meng, D.D., J. Kim, and C.J. Kim, *A degassing plate with hydrophobic bubble capture and distributed venting for microfluidic devices*. Journal of Micromechanics and Microengineering, 2006. 16(2): p. 419-424.
48. Kralj, J.G., H.R. Sahoo, and K.F. Jensen, *Integrated continuous microfluidic liquid-liquid extraction*. Lab on a Chip - Miniaturisation for Chemistry and Biology, 2007. 7(2): p. 256-263.
49. Kamitani, A., S. Morishita, H. Kotaki, and S. Arscott, *Improved fuel use efficiency in microchannel direct methanol fuel cells using a hydrophilic macroporous layer*. Journal of Power Sources, 2009. 187(1): p. 148-155.
50. Paust, N., S. Krumbholz, S. Munt, C. Mueller, P. Koltay, R. Zengerle, and C. Ziegler, *Self-regulating passive fuel supply for small direct methanol fuel cells operating in all orientations*. Journal of Power Sources, 2009. 192(2): p. 442-450.
51. Meng, D.D., T. Cubaud, C.M. Ho, and C.J. Kim, *A methanol-tolerant gas-venting microchannel for a microdirect methanol fuel cell*. Journal of Microelectromechanical Systems, 2007. 16(6): p. 1403-1410.
52. Muzychka, Y.S. and M.M. Yovanovich, *Laminar Forced Convection Heat Transfer in the Combined Entry Region of Non-Circular Ducts*. ASME Journal of Heat Transfer, 2004.
53. Churchill, S.W., *FRICTION-FACTOR EQUATION SPANS ALL FLUID-FLOW REGIMES*. Chemical Engineering (New York), 1977. 84(24): p. 91-92.
54. Hetsroni, G., A. Mosyak, E. Pogrebnyak, and Z. Segal, *Heat Transfer of gas-liquid mixture in micro-channel heat sink*. International Journal of Heat and Mass Transfer, 2009. 52: p. 3963-3971.
55. Wong, H., C.J. Radke, and S. Morris, *The motion of long bubbles in polygonal capillaries, part 2 Drag, fluid pressure and fluid flow*. Journal of Fluid Mechanics, 1995. 292: p. 95-110.
56. Hazel, A.L. and M. Heil, *The steady propagation of a semi-infinite bubble into a tube of elliptical or rectangular cross-section*. Journal of Fluid Mechanics, 2001. 470: p. 91-114.
57. Betz, A. and D. Attinger, *Can Segmented Flow Enhance Heat Transfer in Microchannel Heat Sinks?* International Journal of Heat and Mass Transfer, accepted, March 2010.
58. Ajaev, V. and G.M. Homsy, *Modeling Shapes and Dynamics of Confined Bubbles*. Annual Review of Fluid Mechanics, 2006. 38: p. 277-307.
59. Miyamoto, M., Y. Katoh, J. Kurima, S. Kurihara, and K. Yamashita, *Free convection heat transfer from vertical and horizontal short plates*. International Journal of Heat and Mass Transfer, 1985. 28(9): p. 1733-1745.
60. Gunther, A. and K.F. Jensen, *Multiphase microfluidics: from flow characteristics to chemical and material synthesis*. Lab on a chip, 2006. 6: p. 1487-1503.
61. de Gennes, P.-G., F.-C. Brochard-Wyart, and D. Querae, *Capillarity and Wetting Phenomena: Drops, Bubbles, Pearls, Waves*. 2003, Springer: New York. p. 107-151.
62. Xu, J., R. Vaillant, and D. Attinger, *Porous membrane for gas removal in microfluidic channels: physical mechanisms and design criteria*. Microfluidics and Nanofluidics, accepted March 2010.
63. Hermann, H., W. Pitschke, and N. Mattern, *Surface Roughness of Porous Materials and Its Characterization by X-Ray Absorption Measurements*. Physica Status Solidi (a), 1992. 132(1): p. 103-114.
64. Slavchov, R., B. Radoev, and K.W. Stockelhuber, *Equilibrium profile and rupture of wetting film on heterogeneous substrates*. Colloids and Surfaces A: Physicochemical and Engineering Aspects, 2005. 261(1-3): p. 135-140.
65. Duursma, G.R., K. Sefiane, and S. David, *Advancing and receding contact lines on patterned structured surfaces*. Chemical Engineering Research and Design, 2009.